



Photoelectrochemical properties of WO₃ nanoparticulate thin films prepared by carboxylic acid-assisted electrodeposition

W.L. Kwong^{a,*}, A. Nakaruk^{a,b}, P. Koshy^a, C.C. Sorrell^a

^a School of Materials Science and Engineering, University of New South Wales, Sydney, NSW 2052, Australia

^b Department of Industrial Engineering, Faculty of Engineering, Naresuan University, Phitsanulok 65000, Thailand

ARTICLE INFO

Available online 9 April 2013

Keywords:

WO₃ thin films
Electrodeposition
PTA
Photocurrent
Carboxylic acids

ABSTRACT

Optimisation of particle sizes of WO₃ films is important for photoelectrochemical applications. However, most of the developed size-controlled synthesis techniques involve complicated instruments or vacuum systems. The present work presents an alternative method using carboxylic acid-assisted electrodeposition where WO₃ thin films were deposited from peroxotungstic acid (PTA) solution containing different carboxylic acids (formic, oxalic, citric). The effects of carboxylic acids on the electrodeposition and the resultant morphological, mineralogical, optical, and photoelectrochemical properties of the WO₃ films were investigated. The analysis showed that the films consisted of equiaxed nanoparticulate monoclinic WO₃. The deposition thicknesses and the average grain (individual particle and agglomerate) sizes of the films were dependent on the amount of hydronium ions and the molecular weight and associated sizes of the conjugate bases released upon the dissociation of carboxylic acids in the PTA solutions, which result in hydrogen bond formation and molecular dispersion. The photocurrent densities of the films deposited with carboxylic acids were greater than that of the film deposited from pure PTA. These differences were attributed to improvements in (1) grain size, which controls photogenerated electron-hole transport, and (2) effective grain boundary area, which controls the numbers of active reaction sites and electron-hole recombination sites.

© 2013 Elsevier B.V. All rights reserved.

1. Introduction

Photoelectrochemical (PEC) hydrogen production is one of the most attractive and environmentally sustainable methods to harvest and convert solar energy to chemical energy, which is stored in the form of H₂ fuel. WO₃ is an *n*-type semiconductor, which has been investigated for various applications such as photocatalysis [1], gas sensing [2,3], electrochromism [4], electrodes for lithium ion batteries [5], and PEC water splitting [6]. WO₃ has great potential for photoelectrochemical applications owing to its high stability against both corrosion and photocorrosion and its relatively small optical indirect band gap [7,8], which permits limited light absorption in the visible range.

Compared to their bulk counterparts [9], nanomaterials as photoelectrodes for PEC cells are advantageous owing to their superior physical properties, including (1) higher surface area to volume ratio, which increases the number of reaction sites for water photolysis; (2) suppressed charge carrier recombination rates, since photogenerated holes are more likely to diffuse to the photoanode/electrolyte interfaces before recombination in nanomaterials with sizes smaller than their hole diffusion lengths [10] (the hole diffusion length of WO₃ is ~150 nm [11]); and (3) enhanced optical absorption, which

results from increased optical path length by incident light scattering, caused by the change of refractive indices at the boundaries of grains of different orientations [9,10]. However, grain boundaries also act as transportation barriers to photogenerated electron-hole pairs and so it is essential to optimise the sizes of the nanomaterials by varying the synthesis parameters in order to obtain optimal photoelectrochemical performance.

Controlling the size of WO₃ nanostructures has been done using techniques such as hydrothermal [12], sol-gel [13], hot-wire chemical vapor deposition [14], arc discharge deposition [3], radio-frequency magnetron sputtering [15], and organic compound-assisted wet chemical techniques [16–18]. The latter have shown considerable promise as economical and uncomplicated routes for size-controlled synthesis of WO₃ nanostructures. Sun et al. [16] used colloidal processing at high oxalic acid concentrations in tungstic acid to produce smaller grain sizes and lower crystallinities of WO₃ thin films. Meda et al. [18] reported the size-tuning of WO₃ grains prepared by a proton exchange resin method through the addition of various organic dispersants, including ethylene glycol, polyethylene glycol, Igepal®, Brij®, and sugars, where the grain sizes decreased with increasing molecular weight of the dispersant.

To date, the number of investigations on the size-controlled wet chemical synthesis of WO₃ thin films using organic compounds is limited and so the mechanisms related to the growth of nanoparticles have not been explained clearly. The present work reports the

* Corresponding author. Tel.: +61 2 9385 4421; fax: +61 2 9385 6565.
E-mail address: w.l.kwong@student.unsw.edu.au (W.L. Kwong).

electrodeposition of WO_3 thin films with varied grain sizes using peroxotungstic acid solutions containing different carboxylic acids. The effects of carboxylic acids on the electrodeposition and the resultant morphological, mineralogical (phase composition), optical, and photoelectrochemical properties of WO_3 thin films were investigated.

2. Experimental details

Tungsten foils (99.99%, Shanghai Leading Metal, China), 30% w/w hydrogen peroxide (analytical reagent, Univar), and propan-2-ol (99.5% analytical reagent, Univar) were used to prepare peroxotungstic acid (PTA) solutions. The carboxylic acids used were formic acid (99% analytical reagent, Asia Pacific Specialty Chemicals), oxalic acid dihydrate (99.5% Merck), and citric acid monohydrate ($\geq 99\%$ ACS reagent, Sigma-Aldrich).

Detailed preparation procedures of PTA solutions have been reported elsewhere [19]. In brief, 0.03 M carboxylic acids (*viz.*, formic, oxalic, or citric acid) were added to PTA solutions with 0.2 M tungsten and these PTA solutions were used as the electrolytes for film deposition. The films were deposited at room temperature using a three-electrode electrochemical system with fluorine-doped tin oxide on glass (FTO), platinum foil, and Ag/AgCl as the working, counter, and reference electrodes, respectively. All potentials reported refer to the reference electrode. A potential of -0.4 V was applied for times ranging from 15 to 60 min in order to deposit films of varying thicknesses. This deposition potential value was chosen owing to the reduction peak obtained in the linear potential sweeps prior to the deposition process. The as-deposited samples were flushed immediately with distilled water, dried in air, placed on an aluminosilicate brick, and annealed at 450°C in air for 2 h (heating and initial cooling rates of 5°C min^{-1}).

The film thicknesses were determined using focused ion beam milling (FIB; FEI XP200). The microstructures were examined using scanning electron microscopy (SEM; FEI Nova NanoSEM; operating voltage 5 kV). True porosities of the films were investigated using image analysis (*ImageJ*, National Institute of Health). The mineralogies of the unaltered films were determined by X-ray powder diffraction (XRD; Philips X'pert Materials Powder Diffractometer; $\text{Cu K}\alpha$ radiation; 45 kV; 40 mA). Light transmissions were measured using a dual-beam UV–VIS spectrophotometer (Pelkin-Elmer Lambda 35).

The photoelectrochemical properties of the samples were measured at room temperature using the same electrochemical system as described above but using WO_3 thin films on FTO substrates as the working electrodes. The PTA electrolyte solutions were replaced with 0.5 M NaCl aqueous solutions ($\text{pH} = 6.27$). The intensity of incident light (50 W tungsten-halogen lamp, chopped at a frequency of 0.05 Hz) was measured with a light meter (Digitech QM1587) to be ~ 100 mW/cm^2 (light source to sample distance ~ 25 cm). Transient potentiostatic photocurrent measurements were done at a bias potential of 0.7 V. In order to measure the relaxation time of the open-circuit photopotential, the films were pre-treated by biasing at 0.7 V for 1 min under illumination so as to achieve an equilibrium state (as shown by achievement of stable photocurrents) and then left to reach a stationary potential under open-circuit (without bias) and dark conditions. Subsequently, illumination was switched on for the photopotential to reach a stationary value and then off again to measure the time taken for it to decay.

3. Results and discussion

Fig. 1 shows the film thickness variation as a function of deposition times for depositions done in pure PTA and PTA containing carboxylic acids solutions. The film thicknesses were measured from the cross-sections of the films, which were milled by FIB. All films adhered well to the substrates (as shown by the resistance to robust handling) except for those deposited for times longer than 30 min in pure PTA,

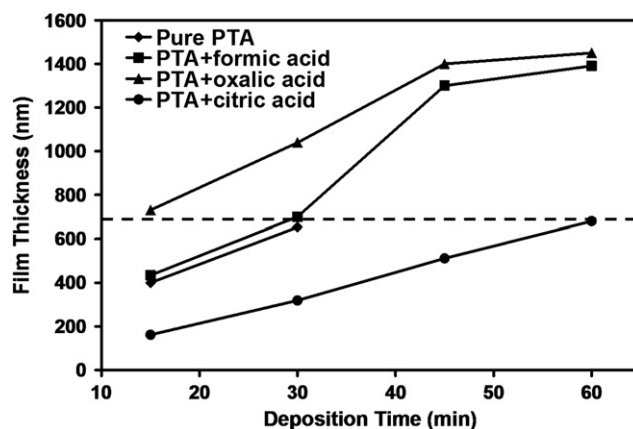


Fig. 1. Thicknesses of WO_3 thin films as a function of deposition times. Dashed line indicates film thickness ~ 700 nm.

which cracked owing to drying stresses. Compared to pure PTA, the deposition thicknesses increased, remained constant, and decreased when the depositions were done from PTA containing oxalic, formic, and citric acids, respectively. Table 1 shows that the same order and the reverse order were seen for the electrolyte conductivities and pH values, respectively. These observations suggest that the deposition thickness is a function of these two variables, which are determined by the hydronium ions and conjugate bases produced upon the dissociation of the acids in aqueous solutions [20].

According to the logarithm of the first proton acid dissociation constant (pK_{a1}), the dissociation of the acids follows in the order oxalic > citric > formic. The small change in the pH of the PTA containing formic acid was caused by the limited dissociation of the acid, which produced a minimal amount of hydronium ions. In contrast, the increase in pH of PTA containing citric acid suggests that the pH was controlled by hydrogen bonding between the relatively large number of highly electronegative oxygen atoms in the citrate ion and the hydronium ions, thereby reducing the availability of hydronium ions. In further contrast, the decrease in pH in PTA containing oxalic acid confirmed the release of a large amount of hydronium ions upon the dissociation of the acid, thereby resulting in high availability of the hydronium ions in the PTA electrolyte despite their formations of hydrogen bonds with the electronegative oxygen atoms in the small oxalate ion. As a consequence of the formation of hydrogen bonds between the hydronium and PTA ions (PTA–hydronium complex ions), a net positive charge developed around the PTA ions, as shown in Fig. 2. This aided the deposition process by driving the PTA–hydronium complex ions to the cathodically biased working electrode, thereby resulting in thicker films deposited from PTA containing oxalic acid. On the other hand, the electrolyte conductivity can be affected by the pK_{a1} values of the acids, which determine the amounts of ions formed in the electrolytes and the molecular weights and associated sizes of the conjugate bases of the acids (in this case the order is citrate > oxalate > formate), which determine the molecular drag in the electrolyte.

The preceding observations show that the relationships between the controlling variables such as pK_{a1} , molecular weight of the conjugate bases, electrolyte pH, and electrolyte conductivity are complex and that the electrodeposition parameter of film thickness cannot be associated independently with them.

Fig. 1 also shows that there was an apparent decrease in the deposition rates at longer times. The main reasons for this were assumed to be the decreasing PTA concentrations during deposition [21,22] and the decreasing electrical conductivities of the films with increasing thicknesses [23].

Since the film thickness is known to influence photoelectrochemical performance [18,19], WO_3 films of similar thicknesses (~ 700 nm),

Table 1

Analytical data obtained for all the samples from the different tests.

Electrolyte composition	Electrolyte pH	κ (mS cm ⁻¹)	t (min)	Grain size* (nm)	Crystallite size^ (nm)	Film strain^ ($\times 10^{-4}$)	(002) peak area	(200) peak area	True porosity (%)	E_g (eV)
0.2 M PTA	1.71	2.900	30	131 \pm 16	107	7	9384	10067	0.87	2.55
0.2 M PTA + 0.03 M formic acid	1.70	3.120	30	94 \pm 12	82	4	7150	4252	1.21	2.70
0.2 M PTA + 0.03 M oxalic acid	1.41	6.570	15	83 \pm 10	92	6	3640	1760	1.91	2.65
0.2 M PTA + 0.03 M citric acid	1.84	0.009	60	45 \pm 4	43	4	6478	9588	2.12	2.63

, electrolyte conductivity; t , deposition time; E_g , optical indirect band gap; * measured from SEM images; ^ measured from Williamson–Hall plots.

deposited for various times from different electrolyte compositions, were characterised further using SEM analysis, XRD analysis, UV–VIS spectrophotometry, and photoelectrochemical measurements.

Fig. 3 shows the surface morphologies of the films. The average sizes of the WO₃ grains (individual particles or agglomerates), measured by the line-intercept method (300,000 \times photographs, 10 lines, 5–10 grains per line), were smaller for the films deposited from PTA containing carboxylic acids compared to that of the film deposited from pure PTA. This was considered to result from the deflocculation and dispersion mechanism of electrosteric stabilisation [24] shown in Fig. 2. The effectiveness of the separation of PTA ions was controlled by the relative availability of hydronium ions for hydrogen bonding with the electronegative oxygen atoms of the PTA ions and the molecular weight and associated sizes of the conjugate bases that occupied the volume of the electrolyte as follows:

- Pure PTA* — Large agglomerates of size ~ 131 nm (~ 500 nm maximum); In pure PTA, the absence of particle separation by any deflocculation mechanism caused solute agglomeration, rapid grain growth, and consequent agglomeration during annealing since the proximity of the ion complexes minimised the diffusion distance.
- PTA containing formic acid* — Small agglomerates of size ~ 94 nm and *PTA containing oxalic acid* — Small agglomerates of size ~ 83 nm; In PTA containing carboxylic acids, with conjugate bases of molecular weights 45 g mol⁻¹ (formate) and 125 g mol⁻¹ (oxalate), the hydronium ions provided a basic deflocculation mechanism of electrosteric stabilisation [24] and the volumes occupied by the conjugate bases in solutions contributed to an increase in the degree of separation of the PTA ions and the resultant diffusion distance.
- PTA containing citric acid* — Individual particles of size ~ 45 nm; In PTA containing citric acid, with conjugate base of molecular weight 209 g mol⁻¹, deflocculation by electrosteric stabilisation occurred but the larger volume occupied by the citrate ions in the solution separated the PTA ions and increased the diffusion distance such that little grain growth took place during annealing.

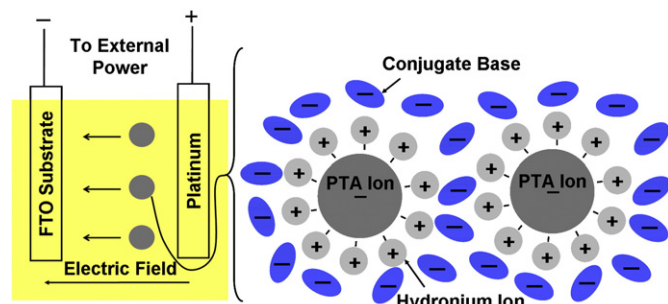


Fig. 2. Schematic diagram of the effects of hydronium ions and conjugate bases on deflocculation and dispersion of PTA ions.

In summary, it can be seen that the use of carboxylic acids is effective in facilitating deflocculation and suppressing solute clustering before electrodeposition. Therefore, the microstructures of the annealed films can be manipulated by using carboxylic acids of different molecular weights and associated sizes of conjugate bases since the sizes of the conjugate bases control the distribution density of the WO₃ nuclei, their proximity, the corresponding diffusion distances, the resultant tendency to undergo grain growth during annealing, and hence their susceptibility to form solid agglomerates.

The true porosity data, which were determined by image analysis, in Table 1 support the preceding conclusions. The film deposited from pure PTA had the lowest true porosity (closed pores only). Even though the agglomerate size was large, delaminations between agglomerates were avoided owing to the strong bonding between the tightly packed agglomerates. In contrast, the films deposited with carboxylic acids exhibited porosities that had been enhanced by delaminations between agglomerates, which resulted from the separation effect of the conjugate bases. Therefore, the true porosity reflects the effect of separation. That is, with PTA containing citric acid (the largest conjugate base), the separation between individual particles was the greatest and so the true porosity also was the greatest. However, delaminations were not visible because the thermal contraction stresses were distributed more evenly across the homogeneous particle array rather than concentrating along inhomogeneously distributed agglomerate boundaries.

Fig. 4 shows the XRD results of the WO₃ thin films. The major peaks for monoclinic WO₃ were present at 23.3°, 23.7°, and 24.4° 2 θ , which correspond to the (002), (020), and (200) planes [25], respectively. The XRD peaks of the films deposited with carboxylic acids were weaker (lower intensities and smaller areas) and broader compared to the film deposited from pure PTA, despite their being of similar thicknesses (the small FTO peaks served as *in situ* normalising standard). The explanations are as follows:

- XRD peak areas*; As shown in Table 1, the XRD peak areas of the films deposited from pure PTA and from PTA containing formic and oxalic acids showed inverse trend with the true porosities and parallel trend with the grain sizes of the films. This was consistent with the beam intensity reduction effect of true porosity (which reduced the area of scanned solid) and the scattering from the agglomerates (which reduced the planarity of the surface profile). Consequently, the XRD peaks of the film deposited from PTA containing citric acid showed anomalously high intensities because, as shown in Table 1 and the preceding text, the true porosity was the highest and agglomerates were absent.
- XRD peak breadths*; The XRD peak breadths of the films depend on the perfection of crystallinity of the individual grains and the randomness of the grain orientations. The Williamson–Hall approach [26] usually is used to determine the crystallite (subgrain) size and this involves measurement of the breadth of the peak at half-height. Table 1 shows that the crystallite sizes and grain sizes were similar, which indicates that the individual grains were single crystals (*i.e.*, no subgrains) and that the image analysis was relatively accurate. The strain values of the films, which

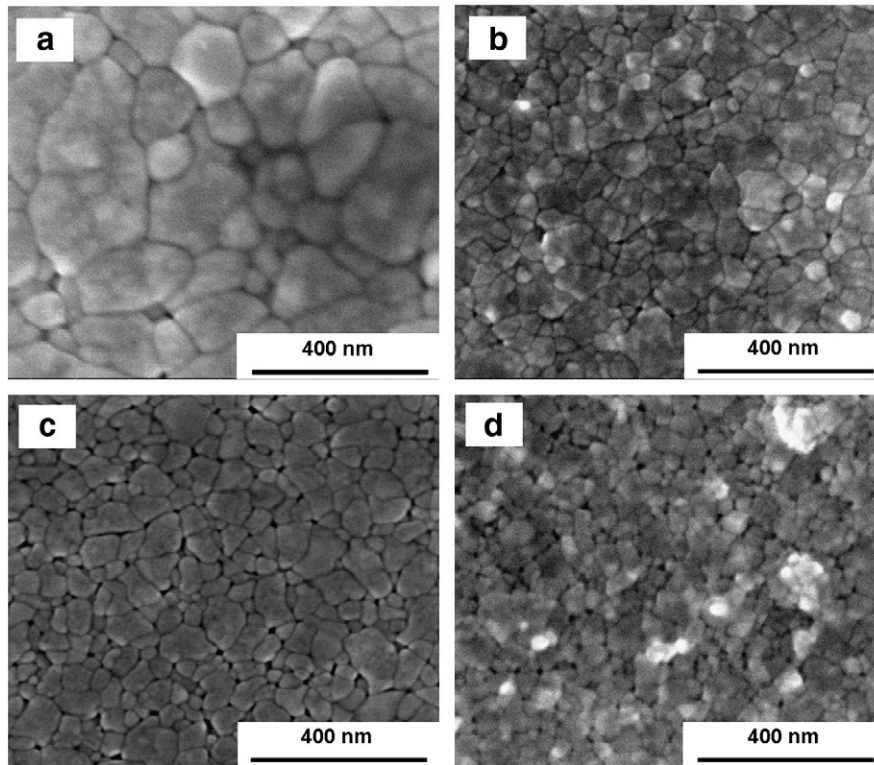


Fig. 3. SEM images of WO_3 thin films deposited from (a) pure peroxotungstic acid (PTA) and (b) PTA with formic acid, (c) PTA with oxalic acid, and (d) PTA with citric acid.

were estimated from the Williamson–Hall plot (not shown), were negligibly small and thus the broadening of the XRD peaks was unlikely to be caused by the strain in the film [26].

Fig. 5 shows the optical transmittance spectra of the films. The transmittance of the films differed marginally in the near-UV (<400 nm) and visible (400–800 nm) regions. The main differences were a small blue-shift (<15 nm) in the optical absorption edge of the films deposited with carboxylic acids (differentiation between these films was ambiguous) and slightly lower optical transmittance of the film deposited with PTA containing citric acid in the visible region. The blue shift was attributed to microstructural defects, as described subsequently. The lower transmittance was attributed to scattering losses resulting from the high true porosity of the film deposited with PTA containing citric acid, as shown in Table 1.

Tauc plots were used to obtain the optical indirect band gaps of the films and the results are shown in Table 1. The optical indirect band gaps of the films varied in the range 2.55–2.70 eV, which is in good

agreement with previous works [27–29]. Since the films showed variations in true porosity (small variation) and grain size (large variation), the associated variation in surface areas would be expected to affect the proportion of surface defects, an increase in which is known to increase the optical band gaps of materials [6,17]. However, the variation between the band gaps, which were determined by a graphical technique involving extrapolation, was too small to differentiate between films.

When a photoanode is in contact with an electrolyte in a dark environment, energy band bending occurs at the photoanode/electrolyte interface in order to achieve thermal equilibrium [30]. On illumination, electron-hole pairs are generated at the photoanode, with the electrons' being excited to the conduction band and the holes' reaching the photoanode/electrolyte interface. This in turn decreases the band bending, where the amount of decrease corresponds to the photopotential [31]. When the illumination is switched off, the photopotential diminishes as the energy band bending is re-established. The relaxation time of the photopotential determines the recombination rate of the photogenerated electron-hole pairs [18].

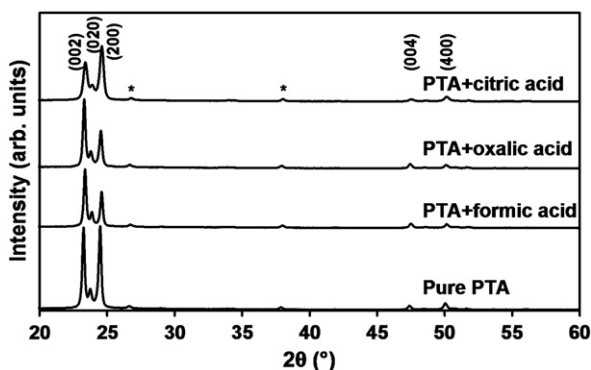


Fig. 4. XRD patterns of WO_3 thin films deposited from different electrolyte compositions. The film thicknesses were ~700 nm for all samples. * marks the FTO peaks.

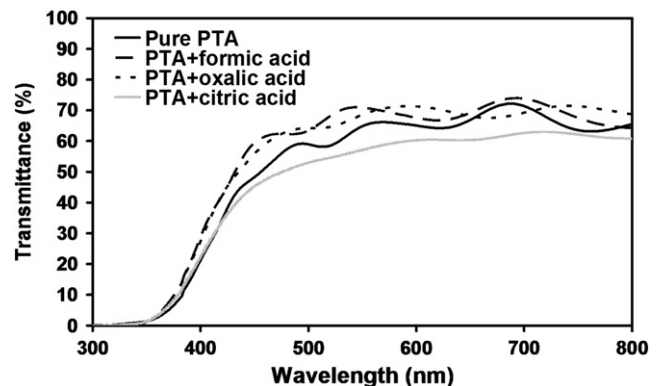


Fig. 5. Optical transmittance spectra of WO_3 thin films deposited from different electrolyte compositions. The film thicknesses were ~700 nm for all samples.

The transient open-circuit photopotential measurements of the films are shown in Fig. 6. The stable potentials attained in the dark were ~ 0.15 V. Once illumination was switched on, the photopotentials developed immediately and then commenced the approach to steady values. The times taken for the photopotentials to decay to their initial value of ~ 0.15 V after the illumination was turned off were ~ 110 s, 160 s, 150 s, and 120 s for the films deposited from pure PTA and PTA with formic acid, oxalic acid, and citric acid, respectively. The relatively long photopotential relaxation times (~ 150 – 160 s) of the films consisting of small agglomerates (~ 83 – 94 nm), which were deposited from PTA containing formic or oxalic acid, suggest that the recombination rates of the photogenerated electron-hole pairs were slow. This was attributed to the relatively short hole diffusion distance to the photoanode/electrolyte interface owing to the small agglomerate sizes. Therefore the photogenerated holes had a higher probability of oxidising water before they could recombine with the photogenerated electrons. The relatively high specific surface area associated with the small agglomerate sizes also may have contributed to the long photopotential relaxation time since this provided a large number of reaction sites for water oxidation. For the film consisting of individual particles, which was deposited from PTA containing citric acid, the large grain boundary area associated with the small particle sizes resulted in a high fraction of surface defects (*viz.*, dangling bonds), which acted as electron-hole recombination sites [32]. In addition, the grain boundaries also act as weak links that hindered electron transport to the back contact (substrate) [33], thereby increasing the recombination rate.

Fig. 7 shows the transient photocurrent densities of the films measured under a tungsten-halogen lamp at an applied potential of 0.7 V. The trend of the photocurrent densities was in the same order as the photopotential relaxation times. This suggests that, as expected, the photocurrent density measurements were dominated by the photogenerated electron-hole separation rate, which depended on the electron transport, the hole transport, the number of reaction sites for water oxidation, and the number of electron-hole recombination sites. The maximal photocurrent density, which was measured in the film consisting of small agglomerates (deposited from PTA containing oxalic acid), was an outcome of a positive balance of these preceding factors.

The measurement for 2 h of the transient photocurrent densities of the films deposited from pure PTA (lowest photocurrent density) and PTA containing oxalic acid (highest photocurrent density) is shown in Fig. 8. The photocurrent density of the film deposited from pure PTA remained stable at ~ 0.06 mA cm $^{-2}$ throughout the measurement. The film deposited from PTA containing oxalic acid showed a decrease in the photocurrent density from ~ 0.135 mA cm $^{-2}$ to ~ 0.110 mA cm $^{-2}$ ($\sim 19\%$) after an hour of measurement and remained stable for the rest

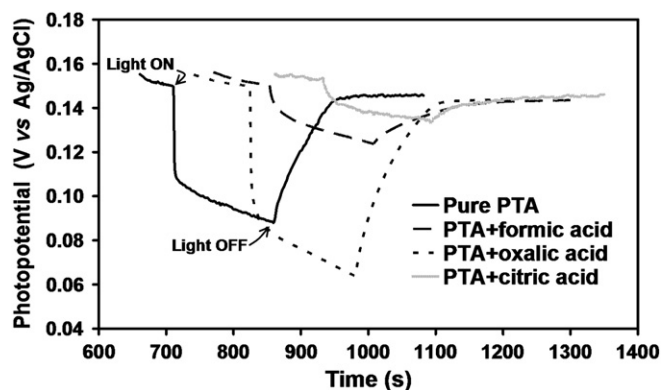


Fig. 6. Transient open-circuit photopotential measurements of WO_3 thin films deposited from different electrolyte compositions. The film thicknesses were ~ 700 nm for all samples.

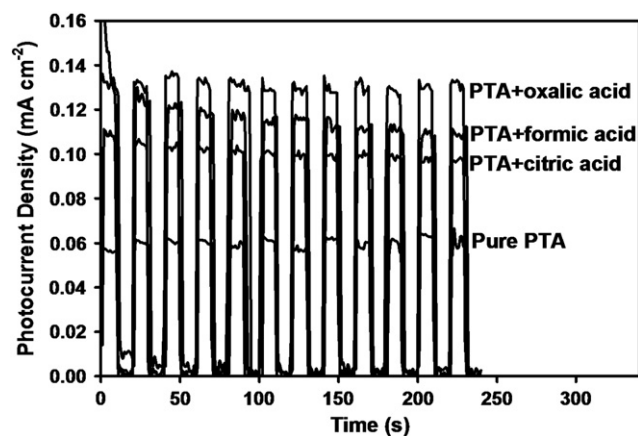


Fig. 7. Transient photocurrent measurement of WO_3 thin films deposited from different electrolyte compositions. The film thicknesses were ~ 700 nm for all samples.

of the measurement. Overall the films demonstrated stability as photoanodes for photoelectrochemical cells.

It may be noted that, as observed before [34,35], the photocurrent densities increased linearly with increasing light intensity, which was varied in the range 30 – 100 mW cm $^{-2}$ (data not shown). It is well known that photon absorption; which depends on the light intensity, absorption edge, transmission, and reflection; results in the generation of electron-hole pairs, which dominates the photoelectrochemical performance [34,35].

Hong et al. [12] and Li et al. [36] reported grain size control (~ 25 – 500 nm) of WO_3 films using post-deposition thermal treatment methods, where the maximal photoelectrochemical performances were observed in the films consisting of apparently small agglomerates of ~ 60 nm. They obtained maximal photocurrent densities of 0.4 – 0.8 mA cm $^{-2}$ at an applied potential of ~ 0.7 V vs. Ag/AgCl, by using a xenon lamp (100 mW cm $^{-2}$) as a light source. Also, other researchers [1,37] had observed photocurrent densities of WO_3 nanoporous films in the range ~ 3 – 6 mA cm $^{-2}$ under identical measurement conditions.

It should be noted that the photocurrent densities in the present work are not directly comparable with those using other light sources, such as a xenon lamp, since different light sources produce different spectral outputs [38]. However, the results from different light sources can be converted approximately using an integrated intensity-wavelength conversion [19]. Using this, the equivalent photocurrent densities for the present samples were in the range ~ 3.0 – 6.5 mA cm $^{-2}$.

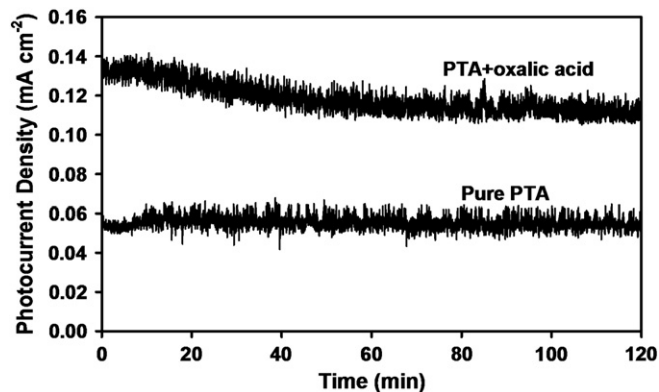


Fig. 8. Transient photocurrent measurement of WO_3 thin films deposited from pure PTA and PTA containing oxalic acid. The film thicknesses were ~ 700 nm for both samples.

The present work and that of others [12,36] show that small agglomerates appear to offer a means of optimising the concurrent factors that affect the photoelectrochemical properties of the films.

4. Conclusions

WO₃ thin films can be electrodeposited from PTA electrolyte solutions in the absence and presence of carboxylic acids. The film deposition thicknesses were influenced by the PTA electrolyte pH and conductivity, which were influenced by the amount of hydronium ions and the size of the conjugate bases of the dissociated carboxylic acids. The pK_{a1} values determined the degrees of acid dissociation while the sizes of the conjugate bases determined the molecular drag in the electrolyte. However, the relationships between the controlling variables such as pK_{a1}, molecular weight of the conjugate bases, electrolyte pH, and electrolyte conductivity were complex and so the film thickness cannot be associated independently with them. The average grain sizes of the films deposited from pure PTA and PTA containing formic, oxalic, and citric acids were 131 nm (large agglomerates), 94 nm (small agglomerates), 83 nm (small agglomerates), and 45 nm (individual particles), respectively. The grain sizes of the films were attributed to the separation of the PTA ions by the conjugate bases and the corresponding diffusion distance. The photocurrent densities of the films deposited with carboxylic acids were greater than that of the film deposited from pure PTA. These differences were attributed to improvements in (1) grain size, which controls photogenerated electron-hole transport, and (2) effective grain boundary area, which controls the numbers of active reaction sites and electron-hole recombination sites.

Acknowledgments

This work was supported in part by a project funded by the Australian Research Council (ARC). The authors are grateful for the characterisation facilities from the Australian Microscopy & Microanalysis Research Facilities (AMMRF) node at the University of New South Wales (UNSW). W.L. Kwong gratefully acknowledges the receipt of UNSW International Postgraduate Award and Postgraduate Research Support Scheme.

References

- [1] A. Watcharenwong, W. Chanmanee, N.R. de Tacconi, C.R. Chenthamarakshan, P. Kajitvichyanukul, K. Rajeshwar, *J. Electroanal. Chem.* 612 (1) (2008) 112.
- [2] X.P. Shen, G.X. Wang, D. Wexler, *Sensors Actuators B* 143 (1) (2009) 325.
- [3] F. Fang, J. Kennedy, J. Futter, T. Hopf, A. Markwitz, E. Manikandan, G. Henshaw, *Nanotechnology* 22 (33) (2011) 335702.

- [4] H.M.A. Soliman, A.B. Kashyout, M.S. El Nouby, A.M. Abosehly, *J. Mater. Sci. Mater. Electron.* 21 (12) (2010) 1313.
- [5] W.J. Li, Z.W. Fu, *Appl. Surf. Sci.* 256 (8) (2010) 2447.
- [6] F. Diqarto, A. Dipaola, S. Piazza, C. Sunseri, *Sol. Energy Mater.* 11 (5–6) (1985) 419.
- [7] G. Hodes, D. Cahen, J. Manassen, *Nature* 260 (5549) (1976) 312.
- [8] D.A.H. Hanaor, G. Triani, C.C. Sorrell, *Surf. Coat. Technol.* 205 (12) (2011) 3658.
- [9] Y. Li, J.Z. Zhang, *Laser Photonics Rev.* 4 (4) (2010) 517.
- [10] J.J. Kelly, D. Vanmaekelbergh, *Electrochemistry of Nanomaterials*, Wiley-VCH, Weinheim, 2001.
- [11] M.A. Butler, *J. Appl. Phys.* 48 (5) (1977) 1914.
- [12] S.J. Hong, H. Jun, P.H. Borse, J.S. Lee, *Int. J. Hydrogen Energy* 34 (8) (2009) 3234.
- [13] X.L. Sun, H.T. Cao, Z.M. Liu, J.Z. Li, *Appl. Surf. Sci.* 255 (20) (2009) 8629.
- [14] C.M. White, J.S. Jang, S.H. Lee, J. Pankow, A.C. Dillon, *Electrochem. Solid-State Lett.* 13 (11) (2010) B120.
- [15] R.S. Vemuri, K.K. Bharathi, S.K. Gullapalli, C.V. Ramana, *ACS Appl. Mater. Interfaces* 2 (9) (2010) 2623.
- [16] M. Sun, N. Xu, Y.W. Cao, J.N. Yao, E.G. Wang, *J. Mater. Sci. Lett.* 19 (16) (2000) 1407.
- [17] M. Sun, N. Xu, Y.W. Cao, J.N. Yao, E.G. Wang, *J. Mater. Res.* 15 (4) (2000) 927.
- [18] L. Meda, G. Tozzola, A. Tacca, G. Marra, S. Caramori, V. Cristino, C.A. Bignozzi, *Sol. Energy Mater. Sol. Cells* 94 (5) (2010) 788.
- [19] W.L. Kwong, N. Savvides, C.C. Sorrell, *Electrochim. Acta* 75 (2012) 371.
- [20] J.C. Kotz, P.M. Treichel, J.R. Townsend, *Chemistry and Chemical Reactivity*, Brooks/Cole, Belmont, 2010.
- [21] I. Zhitomirsky, L. Galor, A. Kohn, H.W. Henricke, *J. Mater. Sci. Lett.* 14 (11) (1995) 807.
- [22] I. Zhitomirsky, L. Galor, *Mater. Lett.* 31 (1–2) (1997) 155.
- [23] S. Bijani, L. Martinez, M. Gabas, E.A. Dalchiele, J.-R. Ramos-Barrado, *J. Phys. Chem. C* 113 (2009) 19482.
- [24] C.C. Sorrell, H. Taib, T.C. Palmer, F. Peng, Z. Xia, M. Wei, in: S. Zhang (Ed.), *Biological and Biomedical Coatings Handbook: Processing and Characterization*, vol. 1, CRC Press, Boca Raton, 2011, p. 81.
- [25] P.M. Woodward, A.W. Sleight, T. Vogt, *J. Phys. Chem. Solids* 56 (10) (1995) 1305.
- [26] S.T. Tan, B.J. Chen, X.W. Sun, W.J. Fan, H.S. Kwok, X.H. Zhang, S.J. Chua, *J. Appl. Phys.* 98 (2005) 013505.
- [27] L. Weinhardt, M. Blum, M. Bar, C. Heske, B. Cole, B. Marsen, E.L. Miller, *J. Phys. Chem. C* 112 (8) (2008) 3078.
- [28] B. Yang, P.R.F. Barnes, W. Bertram, V. Luca, *J. Mater. Chem.* 17 (26) (2007) 2722.
- [29] Y. Sun, C.J. Murphy, K.R. Reyes-Gil, E.A. Reyes-Garcia, J.M. Thornton, N.A. Morris, D. Rafferty, *Int. J. Hydrogen Energy* 34 (20) (2009) 8476.
- [30] E.L. Miller, *On Solar Hydrogen and Nanotechnology*, John Wiley & Sons, Singapore, 2009.
- [31] C.A. Grimes, O.K. Varghese, S. Ranjan, *Light, Water, Hydrogen. The Solar Generation of Hydrogen by Water Photoelectrolysis*, Springer Science+Business Media, New York, 2008.
- [32] B.G. Yacobi, *Semiconductor Materials: An Introduction to Basic Principles*, Kluwer Academic/Plenum, New York, 2003.
- [33] J.K.F. Yau, C.C. Sorrell, *Physica C* 282–287 (1997) 2563.
- [34] H. Wang, T. Lindgren, J. He, A. Hagfeldt, S.E. Lindquist, *J. Phys. Chem. B* 104 (2000) 5686.
- [35] N. Naseri, S. Yousefzadeh, E. Daryaei, A.Z. Moshfegh, *Int. J. Hydrogen Energy* 36 (2011) 13461.
- [36] W. Li, J. Li, X. Wang, J. Ma, Q. Chen, *Int. J. Hydrogen Energy* 35 (2010) 13137.
- [37] N.R. de Tacconi, C.R. Chenthamarakshan, G. Yogeewaran, A. Watcharenwong, R.S. de Zoysa, N.A. Basit, K. Rajeshwar, *J. Phys. Chem. B* 110 (50) (2006) 25347.
- [38] W.S. Yoo, K. Kang, *Nucl. Inst. Methods Phys. Res. Sect. B* 237 (1–2) (2005) 12.